STUDY OF STOCHASTIC TOROIDAL FIELD RIPPLE LOSSES OF CHARGED FUSION PRODUCTS AT THE MIDPLANE OF TFTR

R.L. BOIVIN
Plasma Fusion Center,
Massachusetts Institute of Technology,
Cambridge, Massachusetts

S.J. ZWEBEN, R.B. WHITE
Princeton Plasma Physics Laboratory,
Princeton University,
Princeton, New Jersey

United States of America

ABSTRACT. Measurements of charged fusion product losses were obtained near the first wall of TFTR, using a movable detector located just below the outer midplane. Experimental results obtained in MHD quiescent discharges showed the presence of two loss mechanisms — one associated with first-orbit losses and the other believed to be toroidal field stochastic ripple diffusion. Numerical calculations, based on the model of Goldston et al. (Phys. Rev. Lett. **47** (1981) 647), were found to be in reasonable agreement with the experimental results.

1. INTRODUCTION

It is well known that confinement of the fusion produced 3.5 MeV alpha particle is necessary in a fusion reactor for reaching ignition. In addition to the well known first-orbit loss process, one of the possible loss mechanisms originates from the presence of ripples in the toroidal magnetic field (TF). This mechanism has been the subject of theoretical considerations since the early days of tokamak research [1-3]. The experimental results presented in this paper focus on the study of the effects of TF ripple on the confinement of charged fusion products (CFPs), namely the 1 MeV triton and the 3 MeV proton. These two particles are produced in one of the branches of the D-D fusion reaction and, since they have a gyroradius and collisionality rate very similar to those of the 3.5 MeV alpha particle, they serve as test particles in simulating future D-T conditions.

In TFTR (a circular machine), the expected dominant ripple loss mechanism for CFPs is the toroidal field stochastic ripple diffusion which has been theoretically described by Goldston et al. [4] in 1981, but which, so far, has not been observed experimentally. Although this mechanism is expected to cause only small global losses of MeV ions, it could theoretically create local heat loads on the first wall of a tokamak, possibly exceeding the power handling limits in ITER, for example [5]. Fast particles can also be trapped in TF ripple wells (ripple

trapping) and drift out of the plasma. However, this mechanism (important in ITER) cannot be studied with the existing detectors in TFTR and, consequently, will not be reported here.

2. THEORETICAL EXPECTATIONS

2.1. Ripple induced diffusion

The presence of a discrete number of TF coils causes a periodic perturbation, in the form of ripples, in the magnetic field. In the large aspect ratio approximation, the vacuum field can be expressed as

$$B = B_0 \left(1 - \frac{r}{R_0} \cos \theta + \delta(r, \theta) \sin (N\phi) \right) \quad (1)$$

where N is the number of TF coils (for TFTR, N = 20) and $\delta \equiv (B_{max} - B_{min})/(B_{max} + B_{min})$ is the ripple amplitude (average to peak value). Shown in Fig. 1 are the calculated ripple curves (peak to peak, in %) for TFTR [6].

Since the toroidal axisymmetry is broken, the canonical toroidal momentum P_ϕ is no longer conserved and, consequently, the particles experience an additional drift due to the ripples. The only place where the drift would be uncompensated by the rotational transform is at the bounce point of trapped particles; this explains
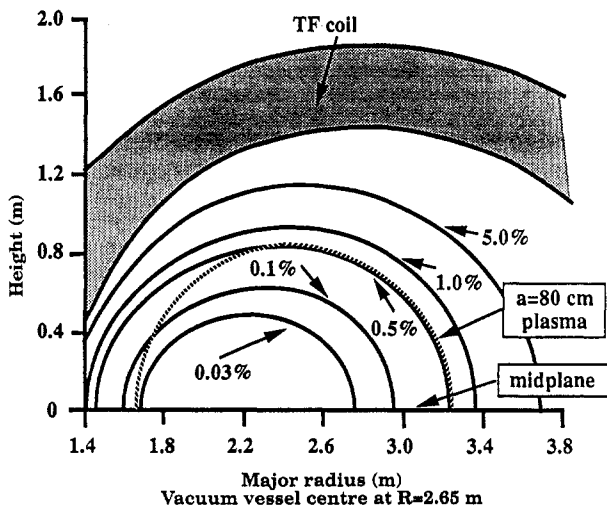
FIG. 1. Vacuum TF ripple curves (peak to peak, in %) for TFTR.

where $q' \equiv dq/dr$. This criterion puts a stringent limit on the maximum ripple strength allowed over the plasma cross-section [11, 7]. Calculations based on an island overlapping threshold criterion were made by Grua and Roubin [12, 13], and also by Duvall [14], and yielded the same parametric dependence within an overall factor of the order of unity (Grua and Roubin found a factor of 1.83). The exact value of the threshold is still under theoretical consideration; this is one of the reasons why this experimental study (see Section 4.2) was undertaken.

Typically, criterion (3) corresponds to a region in the outer part of the plasma, called the ripple stochastic domain (or sometimes the loss domain). Using the vacuum ripple curves for TFTR (see Fig. 1), the loss domain was calculated for a discharge with $I_p = 1.4$ MA, $B_T = 4$ T and $R_0 = 2.60$ m and is shown as the dark area in Fig. 2. Any trapped particle whose bounce point falls in that region will be diffusing at the ripple diffusion rate $D_{ripple} \sim (\Delta r)^2/\tau_b$ and will most likely be lost to the wall. If the loss domain covers a large fraction of the plasma cross-section, this mechanism may theoretically lead to the loss of all trapped CFPs.

The ripple diffusion rate for CFPs is large (at least in TFTR). The step size is of the order of 1 cm near the plasma edge of TFTR and the bounce time is approximately 10 μs. This means that for $\Delta r \sim 1$ cm and

why passing particles are unaffected by the TF ripple. The amplitude of this drift, or its step size, was calculated using a perturbative technique [7] and yielded the following dependence for a circular plasma:

$$\Delta r \simeq \left(\frac{N\pi}{|\sin\theta_b|}\right)^{1/2} \left(\frac{q}{\epsilon}\right)^{3/2} \rho\delta \sin(N\phi_b) \qquad (2)$$

where ρ is the gyroradius and all variables, including the poloidal (θ) and toroidal (ϕ) angles, are evaluated at the bounce point.

With the presence of the $\sin(N\phi_b)$ factor in Eq. (2), the process is not diffusive by itself. At this point, an additional mechanism is necessary to decouple the different radial steps in order to create a diffusive process. This can be done by two very different actions — the first being the effects of collisions (banana drift or ripple plateau regime) and the second being the effect of the toroidal drift (TF ripple stochastic diffusion). Since the collisionality of the CFPs is small, for example the slowing down time of these fast particles approaches one second, the collisionless process will dominate (TF stochastic ripple diffusion). This process will also dominate over ripple trapping losses mainly because the ripple strength is relatively small in TFTR [8-10].

When the ripple strength is too large, the vertical steps (drift) of the particle orbit are decorrelated and the motion becomes stochastic [4]. Stochasticity is consequently present when

$$\delta > \delta_s \equiv \left(\frac{\epsilon}{N\pi q}\right)^{3/2} \frac{1}{(2\rho q')} \qquad (3)$$
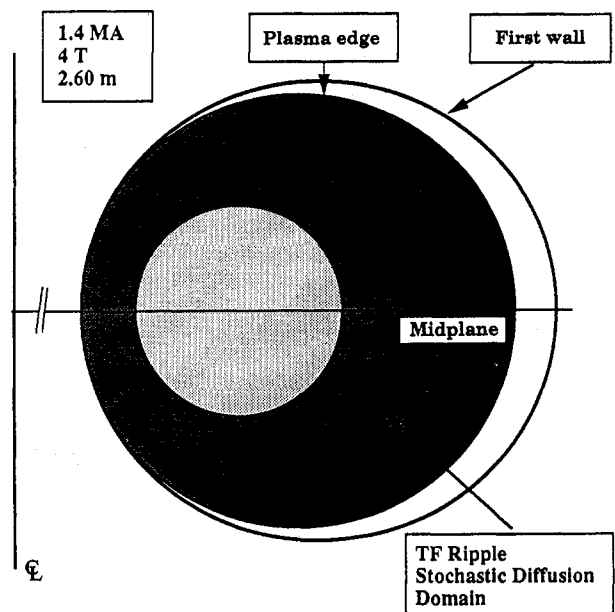

FIG. 2. Ripple stochastic domain in TFTR for a discharge with $I_p = 1.4$ MA, $B_T = 4$ T and $R_0 = 2.60$ m.
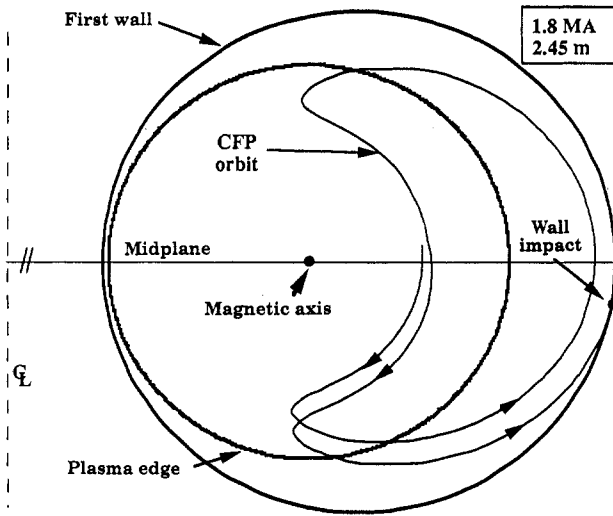
FIG. 3. Poloidal cross-section of TFTR, showing the probable location of impact for a ripple lost particle. The CFP misses the wall on one pass and hits it on the next, just below the outer midplane.

$\tau_b \sim 10~\mu s$, $D_{ripple} \sim 10~m^2/s$. Typically, with such a high diffusion rate, 1 MeV tritons would be lost in less than 10 ms (and three times less for 3 MeV protons), which is more than one order of magnitude smaller than their slowing down time. Consequently, diffusing particles would have nearly their full energy when impinging on the wall.

For a barely confined CFP, just missing the outer midplane wall on one pass (illustrated in Fig. 3), a vertical drift of its bounce point (by 1 cm or so) will cause the particle to hit the wall just below the midplane (or just above it, depending on the ion ∇B drift direction). This highly localized loss of full energy CFPs represents a serious problem of heat loads on the first wall of fusion reactors.

2.2. Loss domains

For a particle of given energy and in an axisymmetric system, any guiding centre orbit can be represented by using its magnetic moment and its radial crossing point on the outer midplane. Shown in Fig. 4 is the distribution of counter-passing particles as a function of their magnetic moment (normalized by $\mu_0 = E/B_0$, where E is the energy of the particle and B_0 is the magnetic field at the magnetic axis) and of the outer midplane crossing point. A similar diagram can be obtained for co-passing particles, for which the inner midplane crossing point is used. Also indicated is the separation

between passing particles (lower left part) and trapped particles (upper right part), referred to as the passing–trapped boundary. When the particle drift (i.e. the banana width) becomes too large, i.e. when it becomes of the order of half of the minor radius, particles will hit the wall (on the lower half of the vacuum vessel in the case of TFTR) on their first poloidal orbit, leading to first-orbit losses. At low current (typically <0.6 MA for TFTR), losses of energetic particles such as CFPs can be quite large (e.g. >50%). Points I and O correspond to barely trapped particles (fattest banana) hitting exactly the inner and the outer midplane wall, respectively.

The presence of the detector near the midplane is illustrated by a trapezoidal area in the trapped particle region. Particles born in that range of r/a and μ/μ_0 can be seen by the detector as first-orbit losses. Diffusing particles (confined on their first orbit) can also be detected if they move in the acceptance area. The width of the acceptance area is defined by the height of the aperture of the detector and is greatly exaggerated in the figure. Note also that the source profile is heavily weighted towards r = 0. Also shown is the region
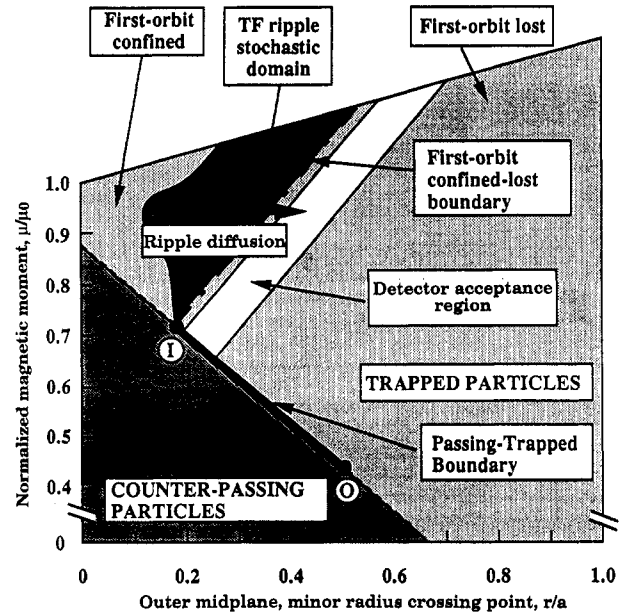

FIG. 4. Distribution of the ripple diffusing particles in μ/μ_0 versus r/a space. Also indicated is the location of the probe detecting area; note that the radial extension of the probe 'sight' view is greatly exaggerated. When the probe is inserted further into the vacuum vessel, its detecting area moves to the left. When the probe passes the radius of the RF limiters, it penetrates into the domain of confined CFPs (upper left corner).

affected by TF stochastic ripple diffusion. At the top
left of the diagram are the trapped particles confined
on their first orbit. Some of them have their bounce
point in the stochastic region and, as shown in the
diagram, will diffuse 'horizontally' (μ/μ_0 being
conserved) until they cross the confined/loss boundary,
either by hitting the wall or by penetrating into the
detector.

2.3. Loss calculations for TFTR

Since the first-orbit loss process occurs very rapidly
(a few microseconds), numerical calculations can be
performed efficiently using an orbit code such as
ORBIT [15]. The problem becomes rapidly more
complex when it is necessary to include diffusive
mechanisms that would bring particles to the wall in
a few hundred to a few thousand transit times (a few
milliseconds), as in TF stochastic ripple diffusion.

Since the detector can measure losses at only one
very specific location, numerical calculations must
include details of the particle impact location, using
sufficiently good statistics. The standard approach is
to numerically solve the CFP guiding centre equations
and to look at the impact of distributions at the wall.
Solving the guiding centre equations already saves a
lot of time compared with solving the complete orbit
(with gyromotion), without losing any physical insight.
The trajectory can be unfolded using the particle guiding
centre Hamiltonian [16, 17] which is based on the
co-ordinates $(r, \theta, \phi, v_\parallel)$. This approach was previously
used by many researchers, also for cases which involved
the presence of TF ripples [9, 18–22]. So far, emphasis
was put on global confinement calculations and on the
poloidal distributions of losses at the wall. This approach
usually includes a detailed and more rigorous physical
description, but uses relatively few particles, typically
~ 1000 or so. However, the previous approach does not
include a calculation of the pitch angle distribution at
the wall, which is measured by the detector. An impor-
tant trade-off arises between the accuracy of the orbit
calculations and the lost particle statistics at the first
wall. Since the interest lies mainly in the pitch angle
distribution of lost particles (at one specific poloidal
and toroidal location), it was decided to increase the
statistics at the first wall, at the expense of details in the
description of the plasma structure (see the Appendix).

As described above, the transition from an oscillatory
type motion to stochastic diffusion has a threshold
character (see Eq. (3)). This criterion for stochasticity,
which can be easily computed, corresponds, for TFTR,
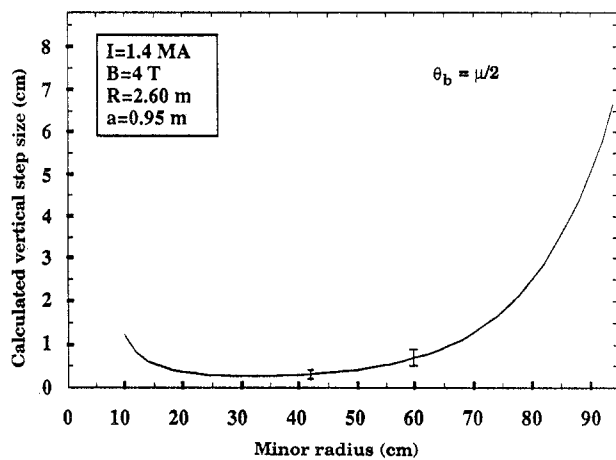to a region located in the outer portion of the plasma

FIG. 5. Vertical position dependence of the ripple step size just
above the plasma centre ($\theta = 90°$) for $I_p = 1.4$ MA, $B_T = 4$ T,
$R_0 = 2.60$ m. The error bars represent the variations due to
uncertainties in the current profile and the ripple amplitude.

(see Fig. 2). A code (MAPLOS) was developed to
calculate the total TF stochastic ripple losses together
with their poloidal and pitch angle distributions at
the wall (see details of the calculations given in the
Appendix). The code starts by calculating the guiding
centre orbits of an ensemble of CFPs (with a birth
distribution uniform in θ, isotropic in $v_\parallel = v \cos\chi$,
and with a radial distribution consistent with the
experimentally found neutron source profile). The
trajectories are followed over a poloidal transit, and
only trapped particles whose bounce points lie in the
stochastic domain are retained for further calculations.
Since the energy and the magnetic moment are conserved,
only the information on the location of the bounce point
is needed. For the diffusion of the bounce point, Eq. (2)
is used. The typical radial dependence of the step size is
shown in Fig. 5 for a particle (a 1 MeV triton) in TFTR
($I_p = 1.4$ MA, $B_T = 4$ T, a = 0.95 m, $R_0 = 2.60$ m),
at a poloidal angle of $\theta_b = \pi/2$. When the particle
approaches the wall, the full guiding centre orbit is
followed in order to check for possible impact. The
particle bounce point is then followed until the particle
hits the wall.

One of the basic results obtained from this code is
shown in Fig. 6, which illustrates the density of bounce
points confined after one poloidal transit (first-orbit
confined). The maximum density is found at a minor
radius of approximately a/3 around $\theta \sim 2\pi/3$. Also
shown is the location of the stochasticity threshold,
indicating where ripple lost particles originate. The
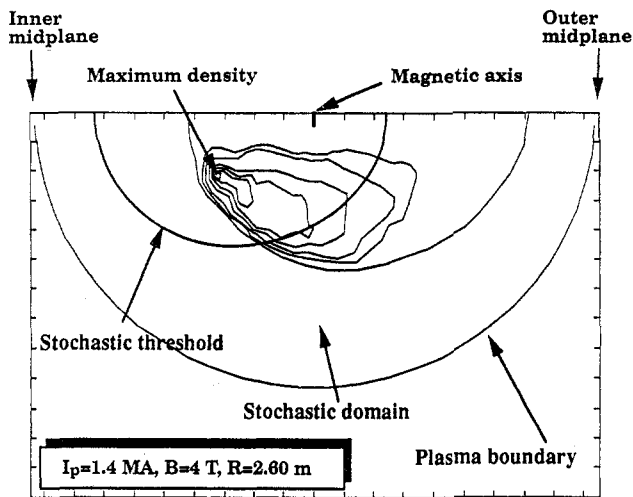global confinement is easily obtained by counting the

FIG. 6. Poloidal density of bounce points for first-orbit confined trapped particles (I_p = 1.4 MA, B_T = 4 T and R_0 = 2.60 m).

number of particles born in the different loss cones. Shown in Fig. 7 are the calculated global fractions of particles lost by first-orbit and stochastic ripple losses versus the plasma current. For both the R_0 = 2.60 m and the R_0 = 2.45 m cases, the first-orbit losses decrease exponentially with current, whereas the ripple losses peak around 1.4 MA. With increasing plasma current, the ripple losses first increase, because the first-orbit confinement of CFPs improves, and then decrease, since the extent of the stochastic domain shrinks; this explains the numerically expected peak in ripple losses. Similar calculations, based only on the extent of the stochastic domain, have also been performed by White and Mynick [11] using the code RIPLOS; this code, however, does not yield any information about the loss distribution at the wall.

As a first approach, the first wall of TFTR was assumed to be toroidally uniform and the aperture of the detector was assumed to be flush with the wall. Later, the presence of the RF limiters was added in the description of the first wall. However, this addition does not solve the problem of the actual detector location (which is, in fact, located radially between the RF limiters and the wall and which has a very small toroidal extension). Also, since the geometry is no longer axisymmetric, the addition of the RF limiters removed a sizable fraction of the much needed statistics. Details of the first wall geometry will be important in a non-circular machine such as ITER [5]. In reactors, the wall heat load could be amplified if losses were not only poloidally but also toroidally localized because of possible sharp edges or prominent surfaces.

As the particle hits the wall, its confinement time is recorded. Shown in Fig. 8 is the calculated confinement time for ripple diffusing particles (expressed as a fraction of the total number of particles). A strong exponential decrease in escaping flux versus particle confinement time was observed. Since both the median and the average confinement times are much smaller than the slowing down time (in this case by two orders of magnitude), it is legitimate to assume that the particle energy is conserved during the ripple diffusion process (impact occurs at full birth energy).
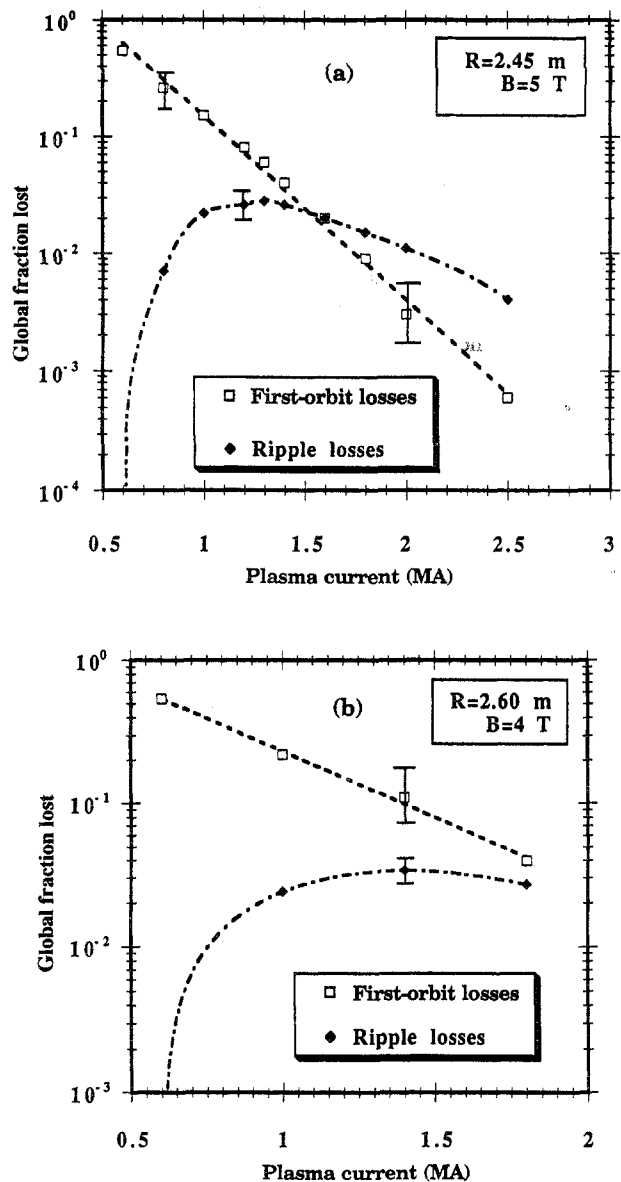

FIG. 7. Calculated total loss fraction versus plasma current for tritons (and protons) and for two different major radii and magnetic fields.
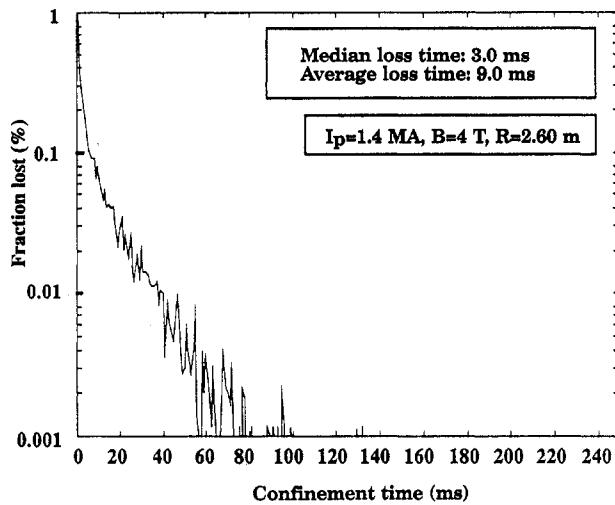
FIG. 8. Calculated distribution of time elapsed before impact for ripple diffusing particles. Escaping particles have an average loss time of 9 ms and a median loss time of 3 ms in the case of $I_p = 1.4\,MA$, $B_T = 4\,T$ and $R_0 = 2.60\,m$.

Once all particles have been followed to the wall, the information on the pitch angle distribution can be readily obtained. For given detector location and plasma conditions, particles detected at different pitch angles correspond to orbits originating from different regions of the plasma. This spatial resolution is especially important when the losses have a spatial character as in the case of first-orbit and TF ripple losses. For first-orbit losses, the pitch angle of maximum flux corresponds to the orbit passing closest to the plasma centre, the source being highly peaked there (see Fig. 4). For medium and high current shots ($\gtrsim 1.0$ MA), this pitch angle corresponds to the fattest banana, at the boundary between passing and trapped orbits. In this case, the bounce points of these orbits are located very near the midplane, on the inner side of the magnetic axis. In comparison, the majority of first-orbit confined particles subject to ripple diffusion originate from a region located just below the magnetic axis (see Fig. 6).

Illustrated in Fig. 9 are the orbits (calculated using the Lorentz code ORBIT [15]) corresponding to peaks in first-orbit and ripple losses. By using energy and magnetic moment conservation, their corresponding pitch angle at the detector (χ_{det}) can be approximated as

$$\mu = \frac{E \sin^2 \chi_{det}}{B_{det}} \tag{4}$$

where

$$B_{det} = \frac{B_0}{1 + \frac{r_{det}}{R_0} \cos(\theta_{det})} \tag{5}$$

is the magnetic field at the detector ($R_0 = 2.65$ m, $r_{det} \approx 100$ cm, $\theta_{det} = -20°$). Since the bounce point of the first-orbit peak is at $\theta = \pi$ and the ripple peak is at $\theta \approx \pi/2$, and since μ and E are conserved, we have

$$\frac{\sin^2 \chi_{det,\,f.o.}}{B_{det}} = \frac{1 - \frac{r_b}{R_0}}{B_0} \quad \text{(first orbit)} \tag{6}$$

$$\frac{\sin^2 \chi_{det,\,ripple}}{B_{det}} = \frac{1}{B_0} \quad \text{(ripple)} \tag{7}$$

where r_b is the minor radius of the bounce point. In this case, $\chi_{det,\,f.o.} \approx 55°$ (at $I_p = 1.4$ MA and $r_b \approx 30$ cm) and $\chi_{det,\,ripple} \approx 65°$. Note, however, that contrary to the first-orbit case (where r_b is a strong function of I_p), the estimate of the pitch angle for ripple losses is independent of the plasma current.

Shown in Fig. 13 (see Section 4.2) are many examples of the calculated pitch angle distribution (from MAPLOS) at the wall (at $\theta = -20°$, the approximate probe poloidal location); in some cases, both peaks are present. The pitch angle resolution of the detector is relatively good, $\pm 3°$ in absolute angle and $\pm 7°$ in peak resolution [8, 23], so the possibility of distinguishing between different loss mechanisms in anticipated. However, in the majority of cases, numerical (and also experimental) results showed that the distribution was usually domi-
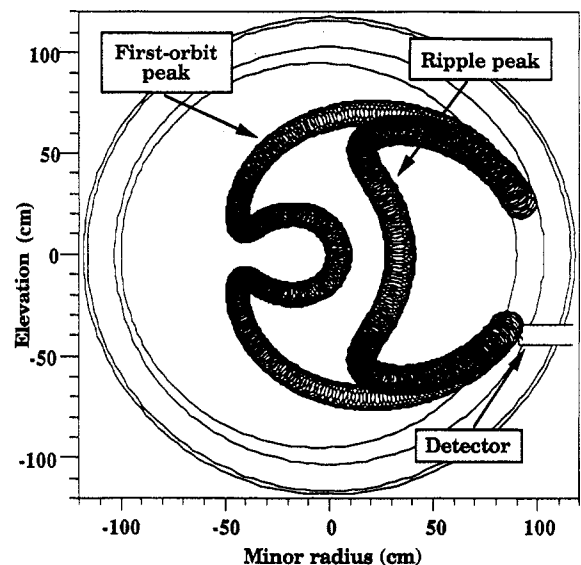

FIG. 9. Comparison of the calculated orbits for peaks in first-orbit and ripple losses for $I_p = 1.4\,MA$, $B_T = 4\,T$ and $R_0 = 2.60\,m$. The pitch angle at the detector is $\approx 55°$ for the first-orbit peak and $\approx 65°$ for the ripple peak.

nated by only one process, thus producing only one peak. It is also important to stress that the calculated ratio of first-orbit losses to TF ripple losses (at the detector) is a function of not only the global fraction lost by either process but also the poloidal distribution of losses on the first wall.

As a bench-mark test, the calculated pitch angle distribution of first-orbit losses obtained with MAPLOS was compared with that obtained with ORBIT [15]. At low current, the agreement between the distributions was found to be within 15% for the flux magnitude and within $\pm 1°$ for the distribution peak. At higher current, some shift ($\lesssim 3°$) was observed. This shift is probably due to the simple expression used in MAPLOS for the magnitude ($|B|$) of the magnetic field, which consists of the TF component only. However, the shape of the curve was found not to be significantly affected; it was only shifted slightly. In addition, the numerical results were compared with the OFMC code [18, 22], written by Tani et al., for typical TFTR cases. Good agreement between the codes was found for all cases studied [9, 10].

3. EXPERIMENTAL TECHNIQUE

The detector is based on a scintillation technique using a ZnS(Ag) phosphor and its design is similar to that of the detectors installed at the bottom of TFTR [24]. A system of collimating apertures, consisting of a pinhole and a slit, disperses incoming particles according to their pitch angle (magnetic moment) and gyroradius (energy) [25]. It is important to note that the restricted range of detectable pitch angles prevents direct measurement of CFP losses through ripple trapping. The detector is mounted on a horizontal movable probe located 35.6 cm below the outer midplane of TFTR ($\simeq -20°$, poloidal angle at the first wall). The detector can span a distance of 23 cm inside the first wall of the vacuum vessel, the outer 9 cm of which lie in the shadow of the RF limiters. These limiters are approximately 50 cm wide (toroidal extension) and located approximately 117° and 171° away toroidally (in the counter-going direction). In these experiments the aperture of the detector was kept behind the RF limiter radius and usually at the same radial location. A different set of experiments was also performed using the motion capability of the probe. These experiments aimed at determining the diffusion rates using shadowing techniques [26]; the results are presented in Ref. [8].

4. EXPERIMENTAL RESULTS

The confinement of CFPs is largely affected by the magnitude of the plasma current and to some extent by the toroidal magnetic field. Because of experimental restrictions from the geometry of the detector aperture, only the dependence on the current could be studied in a sufficiently large range. The moving capability of the detector was used for studying the CFP scrape-off lengths near obstacles. The results of the experiments involving probe motions will be presented elsewhere. The neutral beam power was kept at the minimum ($\lesssim 10$ MW) necessary for an adequate signal (fusion creation rate above $\sim 10^{14}$ s^{-1}), in order to avoid MHD activity, which was absent in all cases except for sawtooth activity (present at higher currents).

4.1. Dependence on the current

The first experimental results were obtained by varying the plasma current with a fixed detector position and a fixed magnetic field. Shown in Fig. 10 is the dependence of the escaping flux on the current, normalized to neutron production, as seen by the midplane detector for two cases with different plasma major radii. It is striking to note that in both cases the dependence on the current is not a monotonic decrease with plasma current. In fact, the experimental curve indicates the presence of a maximum in the detected losses, around 1.4 MA for the $R_0 = 2.60$ m case and around 0.8 MA for the $R_0 = 2.45$ m case. This behaviour indicates the presence of an additional loss process, i.e. one that cannot be explained by a first-orbit loss mechanism alone [24]. This additional loss process is believed to be in large part related to stochastic TF ripple diffusion. The different signatures of the diffusion mechanism will be evaluated in view of the experimental results.

As seen in the previous section, the dependences of both the first-orbit and the ripple loss mechanisms on the current are quite different. However, since CFPs follow curved orbits (e.g. bananas), the midplane detector can only look at a specific region of the plasma. Consequently, global calculations as presented in Fig. 7 cannot be used directly. The code MAPLOS was thus designed to calculate the losses at the wall, at the probe location. Figure 10 shows the current dependence of the total flux measured at the detector (the measured signal is integrated over all pitch angles and gyroradii). In the large plasma case, a very large increase in the detected CFPs can be seen at 1.4 MA. Also plotted are the numerical simulations obtained from MAPLOS using the measured source profile (by the
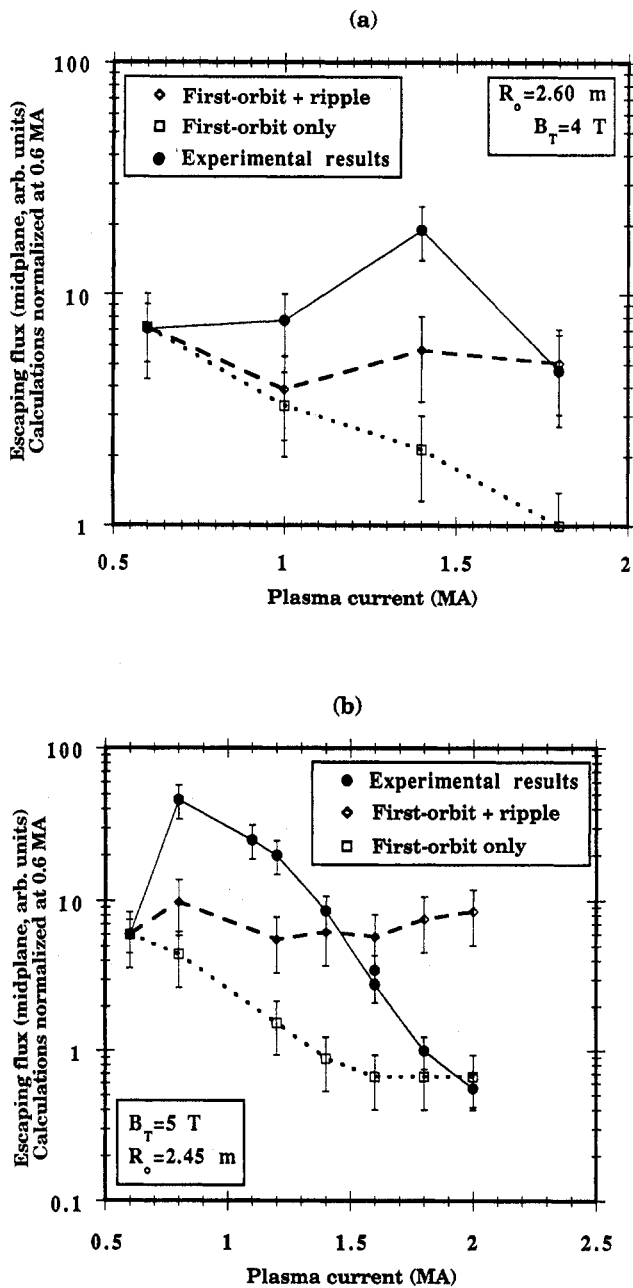
(a)

(b)

FIG. 10. Escaping flux versus plasma current as measured by the midplane detector for two different plasma conditions. The long-dash lines correspond to calculations including first-orbit and ripple losses; the small-dash lines corresponds to first-orbit losses only. The curves are all normalized at 0.6 MA.

neutron multichannel collimator [27]) and the calculated current profile (by the steady state code SNAP [28]). In both cases the curves are normalized at the lowest current point where the losses should be largely dominated by first-orbit losses.

A certain difference between the two cases with different major radii is noticeable. In the case of a 'standard' plasma ($R_0 = 2.45$ m), the transition from first-orbit losses to TF ripple stochastic diffusion occurs at lower plasma current — a behaviour qualitatively expected from Fig. 7. In both cases, the peak in the losses versus the plasma current is totally unexpected from first-orbit considerations only. With the calculations it was possible to correctly predict a local maximum from TF ripple losses, for both cases, although the absolute magnitude could not be reproduced accurately. The reasons for this discrepancy can come from many factors. One of these factors refers naturally to the extent of the knowledge of the profiles — in practice an important source of uncertainty. Another large factor originates from the modelled wall and detector geometries. In the calculations, the flux is taken to impinge on the first wall, not on the detector itself, and the irregularities of the wall are not fully integrated. Since the aperture of the detector is located behind the radius of the RF limiters, some of the flux is expected to be blocked by the limiter before it can reach the aperture. Consequently, the flux would be increasingly reduced at higher current, since the diffusion step size decreases with current (see Eq. (2)).

The difference in major radius is also important. In one case ($R_0 = 2.45$ m) a large vacuum region exists between the plasma and the wall, whereas in the $R_0 = 2.60$ m case the plasma is in contact with the limiters. In the large plasma case the particles experience much larger drift steps (Δr) and so they escape much faster and can be detected much further behind the RF limiters. With decreasing plasma major radius, the drift of CFPs decreases less rapidly (smaller step size) and they have a larger probability of being scrapped off by the RF limiters before they are detected. The effects of the RF limiter shadowing will be studied in the next section (pitch angle distribution) in more detail, since the pitch angle distribution is more focused on individual orbits.

4.2. Pitch angle distribution

The presence of a non-first-orbit loss mechanism is even visible when the pitch angle distribution of the detected CFPs is studied. In the case with maximum losses ($I_p = 1.4$ MA, $R_0 = 2.60$ m), two well resolved peaks with comparable magnitude are present (see Fig. 11). When only a first-orbit loss mechanism is present, only one peak is expected, at the fattest banana pitch angle [24, 29, 30].
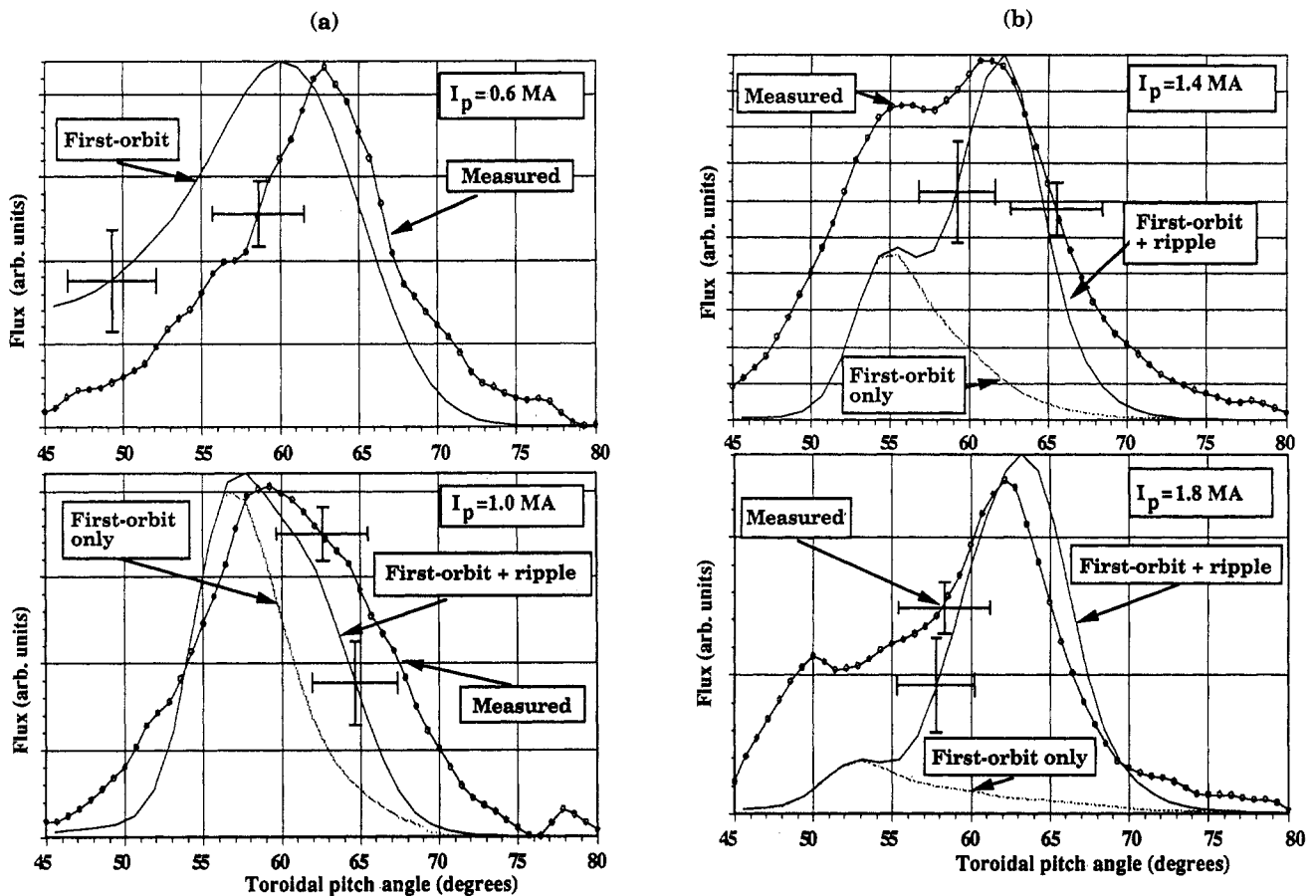
FIG. 11. Measured pitch angle distributions for the current scan at large major radius, compared with MAPLOS calculations.

As seen in Fig. 11 for the 1.4 MA case, the most illustrative cases for the presence of non-first-orbit losses were obtained in the current scan at large major radius (R_0 = 2.60 m). In that scan the features from the first-orbit losses and the ripple losses are clearly distinguishable. The measured pitch angle distributions are shown for four different currents (0.6, 1.0, 1.4 and 1.8 MA, at B_T = 4 T and R_0 = 2.60 m), together with the numerical simulations obtained with MAPLOS. Note that the calculated distributions have been smoothed using a Gaussian distribution with a FWHM measured during calibration [23].

In all cases, the numerical simulations were generally able to reproduce fairly well the measured distributions. The match in peak pitch angles at 1.4 MA and 1.8 MA is especially good. This would indicate the existence of a source of diffusive CFPs that have their banana tips below and above the magnetic axis and would be true for a ripple diffusion mechanism with a stochastic threshold. At 0.6 MA, the match is not as good,

especially at low pitch angles. However, at these lower pitch angles the vignetting effect of the optical components would have to be taken into account and could represent an upward correction of ~50% [8] for the experimental curve. Some of the difference could also be due to the uncertainty in the current profile because SNAP calculations were not available at 0.6 MA (and no sawteeth were present). Other effects, especially the ones related with the RF limiters, will be explored later in this section.

One of the striking features observed during this current scan is the progressive appearance of a second peak. The peak in the pitch angle distribution for the first-orbit losses is expected to move down (in angle) with the plasma current. The maximum in first-orbit losses occurs at the orbit that comes closest to the plasma centre, corresponding to the fattest banana orbit. At 0.6 MA, the peak in first-orbit losses, calculated by ORBIT, occurs at $\chi \approx 57°$ and moves down to $\chi \approx 47°$ for I_p = 1.8 MA; the observed
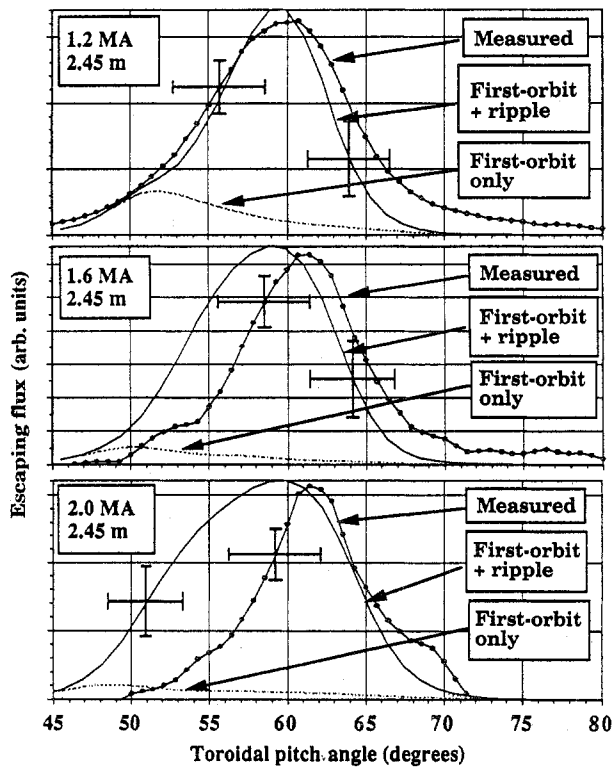
FIG. 12. Comparison of the measured pitch angle distributions with numerical calculations for various plasma currents in a 'standard' plasma $(B_T = 5\ T,\ R_0 = 2.45\ m)$.

variation in the experimental results is shown in Fig. 11. Note, however, that when the optical blurring of the detector system is taken into account, each peak shifts upwards by approximately 3°. In the case of TF ripple losses, the maximum in flux corresponds to the spatial origin of the diffusing particles, not to a specific orbit. Ripple losses should predominantly come from a region just under (or just above) the magnetic axis, where $\theta \approx -\pi/2$ (see Fig. 6). This region of the plasma is connected to the outer wall (near the detector) through an orbit with a pitch angle near 60° at the wall — an orbit which is largely unaffected by changes in the plasma current (see Eq. (7)).

Evidence for the presence of TF ripple losses comes also from the pitch angle distribution found for different plasma conditions. Shown in Fig. 12 are the cases taken with a 'standard' size plasma $(R_0 = 2.45\ m,\ B_T = 5\ T)$ for different currents. Again, it is expected that with increasing plasma current, the peak of the distribution shifts down in pitch angle. In the cases shown, the distributions becomes rapidly dominated by ripple losses above 1.2 MA. Here again, the effects of RF limiters

are still important and will be explored after the discussion of the threshold.

One of the principal characteristics of TF ripple losses is their stochastic threshold. In tokamak geometry, this threshold corresponds (in spatial co-ordinates) to a region called the stochastic domain (see Fig. 2). If this region were covering the whole plasma, the majority of ripple diffusing particles would originate from the vertical chord with the maximum in the density of bounce points (see Fig. 6). In the case shown in Fig. 6, the maximum would correspond to the vertical chord at $R \approx 2.30$ m ($r \approx 35$ cm on the inner side of the magnetic axis). On the other hand, if the threshold were high, the stochastic domain would be limited to a small region in the outer portion of the plasma, i.e. at large major radius. In the latter case, ripple diffusing particles would be detected only at a higher pitch angle and also in considerably smaller number.

The location of the loss domain was changed by artificially varying the coefficient of the stochasticity threshold (Eq. (3)). A coefficient of 1.0 was taken for the threshold derived by Goldston et al. [4]. Grua and Roubin [13], on the other hand, found a relative coefficient of 1.83 for the stochastic threshold. Consequently, the threshold coefficient was varied in the numerical calculations for the $I_p = 1.4$ MA, $R_0 = 2.60$ m, $B_T = 4$ T case discussed above. Shown in Fig. 13 are the results of the simulated pitch angle distributions, compared with the one obtained experimentally (bottom). All parameters of the calculations were kept the same, except for the threshold coefficient, which was varied from 0.3 to 5. The observed changes in the calculated pitch angle distribution are twofold. The first change appears with increasing coefficient, showing the progressive appearance of the first-orbit peak, which eventually dominates. The second change concerns the pitch angle at which the ripple losses peak. In Fig. 13(a) they peak at 59°, whereas at high threshold coefficient (Fig. 13(b)) they peak at 65° — a trend described above using arguments based on the domain location. Compared to the experimental curve (bottom), the conclusion is that within the uncertainty of the measurement and of the calculations (i.e. in considering the error bars in the measured distribution and in the numerical calculations, for both first-orbit and ripple losses), the threshold coefficient must be between 1.0 and 3.0, which is reasonably consistent with the theoretical expectations. It is also interesting to notice that the confinement of trapped particles (excluding the first-orbit lost CFPs) changes from 56% losses (at 0.3 for the threshold coefficient) to only 1% losses (at 5.0). In the range found above, the fraction of trapped
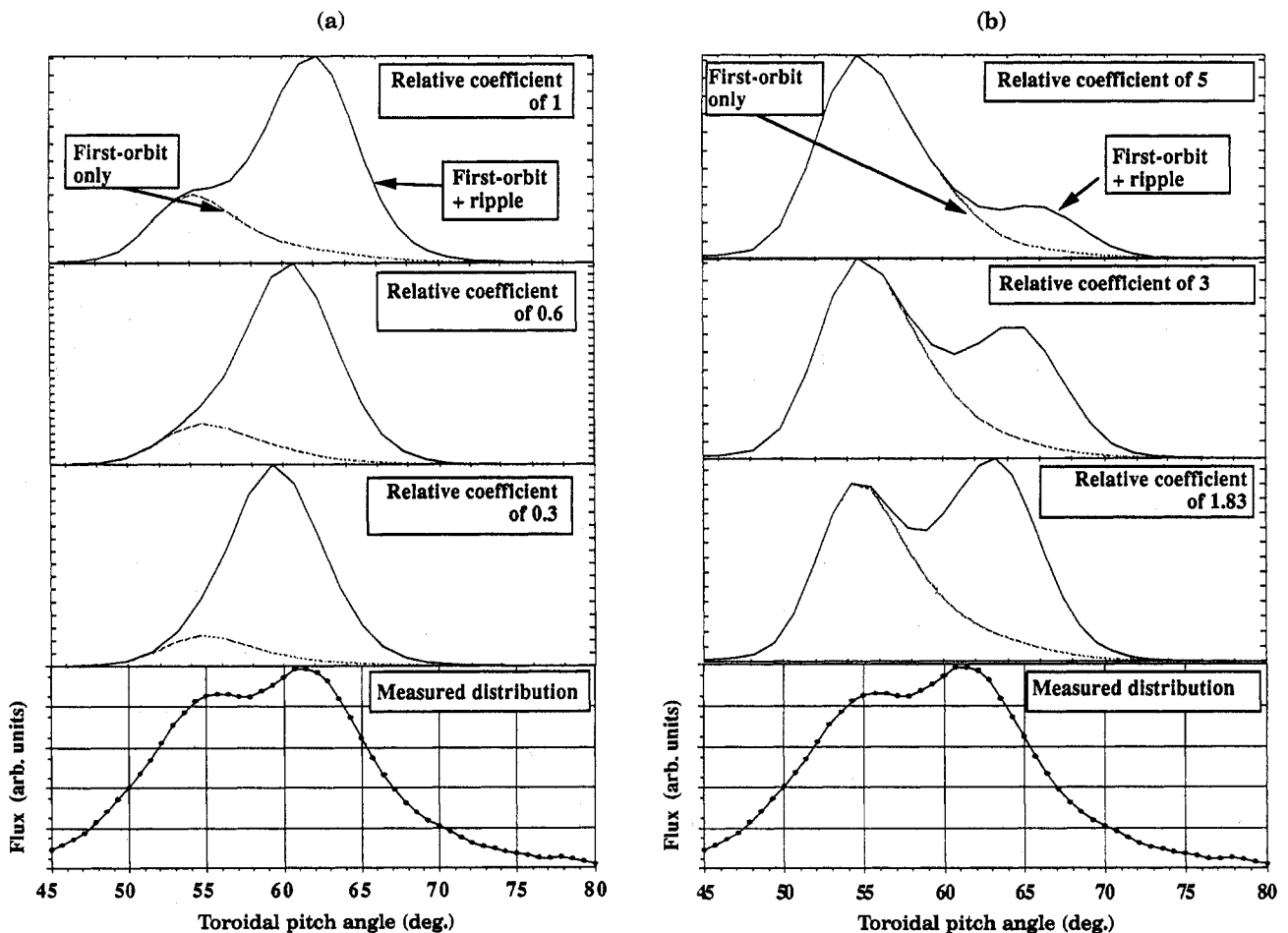
FIG. 13. Effects of variation of the stochastic threshold coefficient on the calculated pinch angle distribution. The threshold of Goldston et al. [4] has a relative coefficient of 1. The coefficient was varied from 0.3 to 5, all other parameters were kept constant.

particles lost is 17% for the coefficient of 1.0 and 3.3% for the coefficient of 3.0.

As mentioned in the preceding sections, the predominant uncertainty in the numerical simulations lies in the description of the first wall geometry, especially when considering the RF limiters. In MAPLOS, the limiters were added and the first wall was taken to be positioned at the location of the aperture of the detector. However, the numerical statistics for the detector were reduced, since the geometry of the system was no longer axisymmetric. Shown in Fig. 14 are the cases presented above, with the RF limiters added to the model geometry of the first wall. Low current cases, which are dominated by first-orbit losses, are naturally not significantly affected by the change. Interesting changes appear in the $R_0 = 2.60$ m case, at $I_p = 1.4$ MA and 1.8 MA, and in the $R_0 = 2.45$ m case, at $I_p = 1.6$ MA

and 2.0 MA, where the ripple peak is reduced, with some diffusing flux being blocked by the limiters. The agreement between calculations and experimental results thus improved significantly with the addition of the RF limiters.

The effects of the RF limiters were investigated by slightly changing the radial position of the detector. The conditions were kept the same ($R_0 = 2.60$ m, $I_p = 1.4$ MA), except for the field, which was slightly smaller (3.5 T instead of 4 T). Shown in Fig. 15 are the measured pitch angle distributions for the scan during which the aperture was moved gradually away from the wall (over 3.5 cm). Also shown are the numerical calculations (including the presence of the limiters) made for the first and the last cases, in which the wall was positioned at the aperture position. All the measured distributions have the same normalization
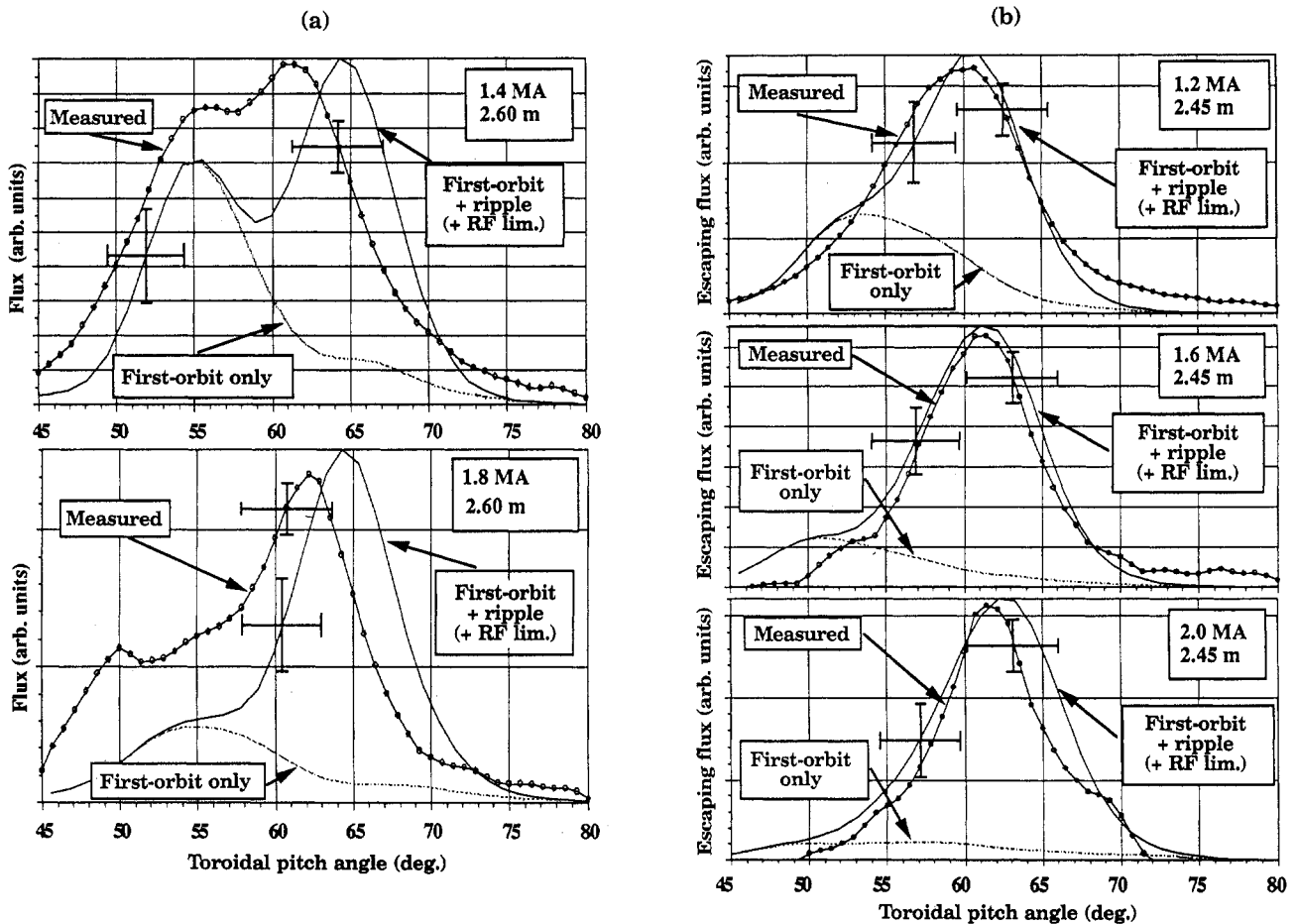
(a)

(b)

FIG. 14. Comparison of the measured pitch angle distributions with numerical calculations including the RF limiters. The first wall is located at the position of the detector aperture.

(normalized by the source strength and for the same camera gain). The first-orbit peak increases very little, whereas the ripple peak at least doubles in amplitude. This difference in behaviour for the two peaks is characteristic of a first-orbit mechanism and a diffusive mechanism [8].

4.3. Poloidal distribution

One of the main motivations for the study of TF ripple losses is the possible occurrence of highly localized losses just below the outer midplane of TFTR. The main difficulty in verifying the expected localization lies in the limited number of detectors that one can put on the first wall. In TFTR there is a total of four detectors on the inner wall. The midplane detector is in a very good position for verification of the presence of ripple losses.

Ripple losses account for ~80% of the losses at 20° below the midplane, where no losses are expected for the other detectors. Such a big difference should be distinguishable when compared with the bottom detectors. However, comparison of the experimental results with the numerical simulations is complicated by several factors.

First, differences in detection and optical efficiencies between the various detectors have to be taken into account [23]. Second, the major uncertainty in these calculations comes from the calculation of the loss distribution; MAPLOS maps the losses on the first wall, not at the detectors themselves. In reality, the detectors stick out somewhat from the first wall (especially the midplane detector). At the very bottom of the machine (bottom detectors) the difference would be quite small, since the orbits are nearly perpendicular
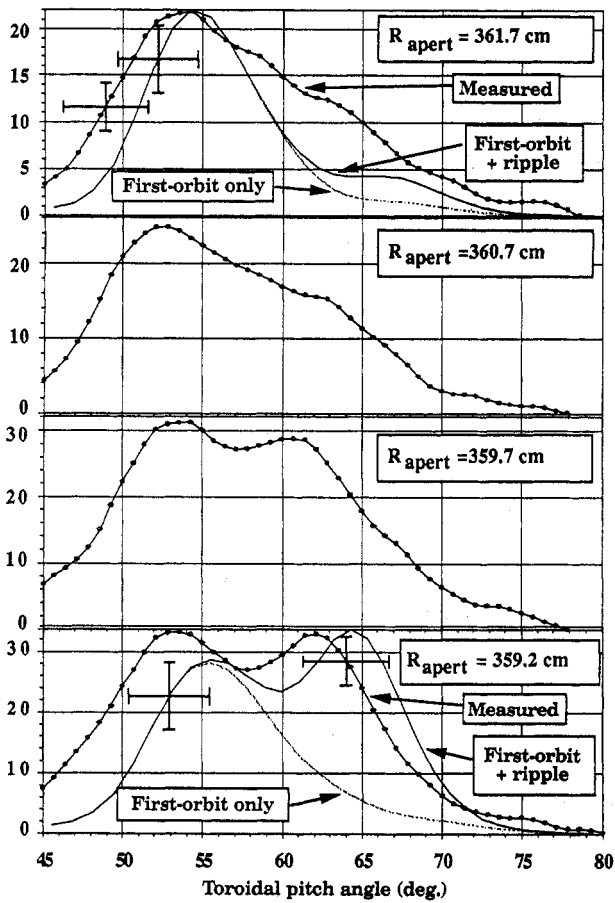
FIG. 15. Pitch angle distributions obtained at decreasing radial positions behind the RF limiters. The experimental results were normalized by the neutron production, and the camera gain remained the same. The ripple peak in (b) doubles in amplitude, whereas the first-orbit peak increases only slightly.

to the wall. However, at the midplane their impact is more tangential. In the latter case, the orbital effects on the calculated flux must be considered.

Figure 16 shows cases taken at different plasma currents. At low current (0.6 MA) the calculated distribution is dominated by first-orbit losses widely spread at the bottom of the vacuum vessel, whereas at high current (1.8 MA) the distribution is very largely dominated by ripple losses localized below the midplane. The points corresponding to the different detectors [23] were added to the numerical curves. The experimental points were normalized to the curve through the result obtained from detector No. 6 located at θ = -90°. Also indicated are the uncertainties in the numerical calculations that were obtained by varying the source and current profiles over a range consistent with the SNAP calculations and the source profile measurements.
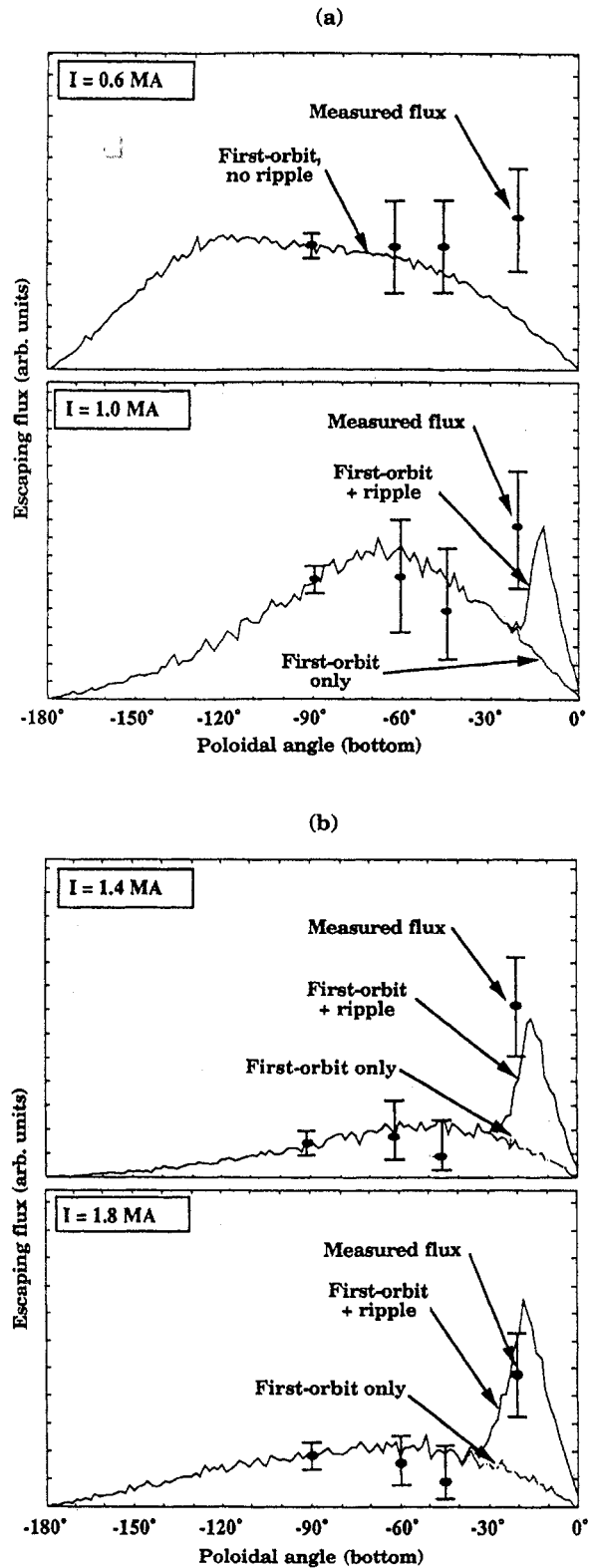

FIG. 16. Poloidal distribution of CFPs at the bottom of TFTR for different plasma currents (B_T = 4 T, R_0 = 2.60 m). The experimental points obtained with the four detectors were added to the numerical calculated distribution (continuous line). The experimental points are normalized at θ = -90°.
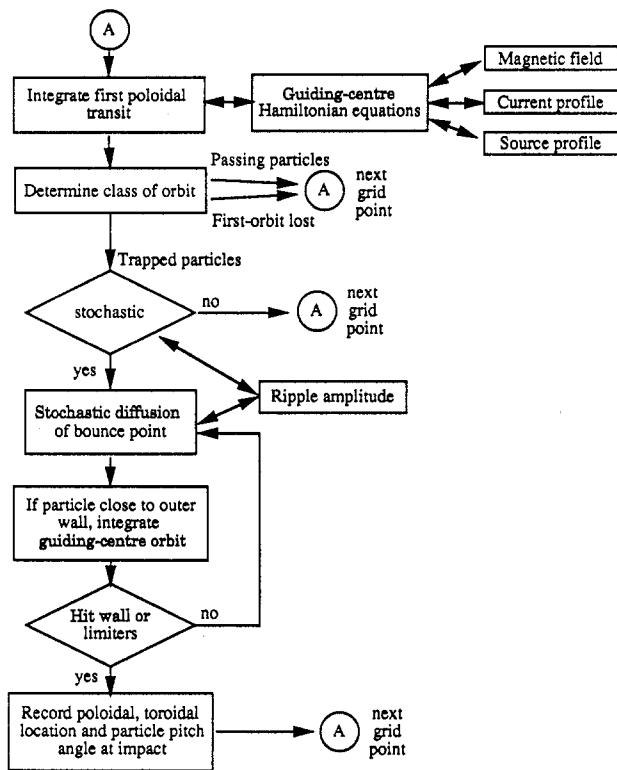
FIG. 17. Block diagram of the code MAPLOS illustrating the algorithm used to calculate TF stochastic ripple losses (see Appendix).

For the current scan shown (R_0 = 2.60 m) there is partial agreement, indicating (especially when considering the error bars) that a peak may occur just below the midplane where ripple losses are expected. The 0.6 MA case is particularly difficult to simulate because of the large Shafranov shifts. With moderate neutral beam injection power levels (necessary for CFP production) the plasma is no longer quite circular (it is elongated in the major radius direction) and is also shifted towards the outer midplane. The first-orbit loss distribution would consequently move considerably towards smaller angles (right hand side of Fig. 16) and change shape (the peaking would also increase somewhat). Because of the major complications that non-concentric, non-circular plasmas produce in the calculations of CFP orbits, these corrections could not be implemented in MAPLOS. These effects are much less severe at higher current.

5. DISCUSSION

Losses of CFPs were measured just below the midplane of TFTR. In addition to first-orbit losses, the

presence of another loss mechanism was observed; this mechanism has many of the characteristics expected from TF stochastic ripple diffusion as described by Goldston et al. [4]. From theoretical considerations, the following signatures of TF stochastic ripple diffusion of CFPs were established:

(a) TF ripple diffusion affects trapped particles only.
(b) Ripple diffusion exhibits a spatially localized stochastic threshold. Diffusing particles are generally deeply trapped (but not ripple trapped).
(c) The diffusion rate is relatively large and the loss time is small compared to the thermalization time.
(d) The losses are localized poloidally (just below the outer midplane).
(e) The losses are strongly dependent on the plasma current.
(f) The diffusion rate is set by external parameters (ripple amplitude, plasma current, plasma major radius, etc.).

Evidence for point (a) was described in Section 4.2 and was also found during shadowing experiments [8]. Particles with large pitch angle (i.e. trapped particles) were found, for example, to diffuse behind the RF limiters. The possibility that non-first-orbit flux was due to diffusing passing particles was excluded, since the pitch angle of the escaping CFPs was clearly away from the passing/trapped boundary (see Fig. 11).

The presence of a well delimited stochastic threshold (point (b)) was demonstrated in Fig. 13 and also in Figs 11 and 12. The clear resolution (Section 4.2), through the pitch angle distribution, of two classes of lost particles was explained by the spatially separated regions of first-orbit losses and ripple losses. Numerical calculations based on the TF ripple diffusion model were able to simulate quantitatively the experimental results. The predictions of the peak in the pitch angle distributions also matched the experimental results over a wide range of plasma conditions. The inclusion of the RF limiters in the calculations improved the agreement between simulation and experiment, especially at higher current where the diffusion rate is smaller.

The presence of a spatially localized threshold prevents many particles from ripple diffusing, especially those near the centre of the plasma; otherwise, they would escape at pitch angles ranging in between the two observed peaks (Fig. 13). These pitch angles correspond to orbits originating from a section of the plasma of minimum ripple amplitude — a region theoretically expected to be free of stochastic ripple diffusion. The experimental results were found to be consistent with the model proposed by Goldston et al.

[4], but also with the more optimistic model of Grua and Roubin [12, 13], which differs by a factor of 1.8 for the stochastic threshold.

Points (c), (d) and (f) are certainly connected. The escaping particles at high pitch angle were detected at their full energy (birth energy). Also, the reproducibility of the results and the consistency of the agreement with theoretical expectations excludes for the majority of the cases studied the possibility of coherent MHD induced diffusion. This is also supported by the fact that when cases that were not low q discharges were studied and when a fast time response was used (with the photomultiplier tubes), no indication of modulated losses (up to 100 kHz) was found. Finally, by using all four detectors, an additional flux was found to reach the wall near the midplane (point (d)), which is at least in qualitative agreement with theoretical simulations.

In Section 4.1 it was shown that the measured losses were at least qualitatively consistent with the presence of ripple diffusing particles, especially because of the observed peak at medium current. This behaviour was found for both aspect ratios (Fig. 10), with the experimental results exhibiting a local maximum as expected from numerical calculations. The measured flux values were clearly different from the calculated values when only a first-orbit loss process was taken into account. For loss mechanisms other than TF ripple diffusion (and first-orbit loss), the losses are not expected to be strongly dependent on the current (point (e)). It is clear that any type of additional losses would be small at low current, since most of the particles are lost on their first orbit. However, at high current, the losses decreased after 1.4 MA, especially in the $R_0 = 2.45$ m case, in which the measured losses decreased significantly with current.

6. CONCLUSION

Using a radially movable detector installed on TFTR, CFP losses were measured just below the outer midplane. Energy, pitch angle (magnetic moment) and time resolved measurements of the escaping flux indicated the presence of an additional loss mechanism on top of the first-orbit loss process. The experimental results were compared with a loss mapping code, and we were able to identify for the first time and with good confidence the presence of stochastic TF ripple diffusion.

One immediate consequence of this experiment concerns the global stochastic TF ripple losses of CFPs in TFTR. The experimental results are consistent with the model of Goldston et al. [4] which predicts a maximum

loss fraction of 5%. This level would be insufficient to explain the observed low triton burnup [31]. This also means that for the D-T phase of TFTR, TF ripple losses should not prevent the study of collective effects from alpha particles.

However, this does not exclude the possibility of synergistic effects, for example between stochastic TF ripple diffusion, ripple trapping, sawteeth and MHD activity. This category of effects would be part of the next logical steps in the study of single-particle confinement of CFPs, especially in TFTR.

Finally, this experiment has long term consequences, namely regarding the design of fusion reactors such as ITER. There is a crucial need to take into account the effects of the stochastic TF ripple diffusion on the design of such reactors. Different threshold coefficients (within a factor of two of the Goldston et al. model) should be considered in numerical analyses. In addition, the delicate problems of first wall heat loads will necessitate a detailed analysis of the interaction of the first wall geometry with ripple losses of CFPs, such as developed here, in the interpretation of the experimental results (MAPLOS).

Appendix

MAPLOS

For a code such as MAPLOS, which aims at calculating fast particle losses, it is important, for obtaining good statistics, to ensure that it is sufficiently fast. First of all, only the guiding centre orbit is integrated, treating gyroradius effects only when close to obstacles (i.e. walls). The calculations use the guiding centre integration routine, developed by White and Chance [16]. Substantial simplifications were introduced by considering circular, concentric (low β) flux surfaces for TFTR geometry. For the problem at hand, the particles remain at fixed energy (monoenergetic and no slowing down) and fixed magnetic moment (no collisions). The action of the TF ripples enters only through the diffusion operator (see Eq. (2)).

Particles were started through a grid of birth locations composed typically of 60 radial, 60 poloidal and 60 pitch angle points (the equivalent of 216 000 particles). The radial and poloidal distributions are uniform in the polar co-ordinate grid. The toroidal location was determined randomly. The birth pitch angle distribution is isotropic and is also slightly jiggled (small perturbations added to the isotropic distribution) in order to prevent aliases

in the resulting distributions. This relatively large number of particles was needed in order to obtain good statistics for the various distributions, especially for the pitch angle distribution, which is calculated at a specific wall location.

The current profile is modelled by a simple parabolic dependence:

$$J(r) = J_0 \left(1 - \frac{r^2}{a^2}\right)^\alpha \tag{A.1}$$

where α is a parameter obtained from SNAP [28] and/or TRANSP [32] calculations. The source profile is usually obtained from the neutron multichannel collimator and can be modelled by a parabolic fit

$$S(r) = S_0 \left(1 - \frac{r^2}{a^2}\right)^\gamma \tag{A.2}$$

or a Gaussian fit

$$S(r) = S_0 \exp\left(-\left(\frac{r}{\sigma}\right)^2\right) \tag{A.3}$$

where γ and σ are obtained from the experimentally found source profile width.

The TF ripple magnitude (see Fig. 1) is taken from a fit [11] to the calculated vacuum ripple [6] and is modelled by

$$\delta = \delta_0 \exp\left(\frac{((R_0 + r \cos\theta - R_{rip})^2 + b_{rip}(r \sin\theta)^2)^{1/2}}{w_{rip}}\right) \tag{A.4}$$

where R_0 is the plasma major radius, $R_{rip} = 2.25$ m is the major radius of the 'centre' of the ripples, $b_{rip} = 1.1$ is the ellipticity and $w_{rip} = 0.185$ m is the ripple scale length.

The block diagram shown in Fig. 17 summarizes the algorithm used in MAPLOS for the calculations of ripple losses. By using the guiding centre equations, the first poloidal transit (also called the first orbit) is derived. At the moment of impact, first-orbit lost particles are eliminated and their impact location recorded. Passing particles are also simply discarded. The remaining particles (trapped, first-orbit confined particles) are separated according to the threshold given by Eq. (3)). From that point, only TF ripple diffusing particles are kept and their bounce point is then followed. Because the expression for the step size (see Eq. (2)) is only valid at $\theta_b \neq \pi$ and $\theta_b \neq 0$, first-orbit confined particles, born in the region very near the midplane (actually a very small number), are also discarded. They are also unlikely to contribute significantly to the measured signal and, naturally, they could be trapped in the ripple well (but could not be detected).

Diffusion of the bounce point is then applied to the particles by using the expression for the step size (see Eq. (2)). In the stochastic ripple regime, the toroidal angle becomes completely random, except very near the threshold. Particles are not allowed to enter the non-stochastic region. They are 'bounced' back towards the edge, inside the stochastic region.

Up to this point, only the bounce point of the diffusing trapped particle was followed. For any positive step size (any increase in minor radius of the bounce point), the particle orbit is then followed from the bounce point up to the midplane. If an impact occurs, the location is recorded; if not, the diffusion resumes until an impact occurs. The wall is usually modelled as a simple circular surface and axisymmetric. However, cases have been run taking into account the presence of the RF limiters in order to explore the effects of the different impact distributions on the wall. Future plans call for the addition of the detector as an obstacle and for calculations of the pitch angle distribution at the detector location, not just at the first wall.

This code was run on the CRAY-2 and took typically between 80 and 130 min for 216 000 grid points. Some exceptions were found at small major radii or when the threshold coefficient was increased artificially (increasing the number of lost particles).

ACKNOWLEDGEMENTS

REFERENCES

[1] ANDERSON, O.A., FURTH, H.P., Nucl. Fusion 12 (1972) 207.

[2] DAVIDSON, J.N., Nucl. Fusion 16 (1976) 731.

[3] GOLDSTON, R.J., TOWNER, H.H., J. Plasma Phys. 26 (1981) 283.

[4] GOLDSTON, R.J., WHITE, R.B., BOOZER, A.H., Phys. Rev. Lett. 47 (1981) 647.

[5]   POST, D.E., BORRASS, K., CALLEN, J.D., et al.,
      ITER Physics, ITER Documentation Series No. 21,
      IAEA, Vienna (1991).

[6]   BROWN, D.I., TFTR Magnetics Handbook, Techn.
      Rep. PPPL-ID-2, Princeton Plasma Physics Laboratory,
      Princeton, NJ (1983).

[7]   WHITE, R.B., Theory of Tokamak Plasmas, North-Holland,
      Amsterdam (1989).

[8]   BOIVIN, R.L., Measurements of Charged Fusion Product
      Diffusion in TFTR, PhD Thesis, Princeton University,
      Princeton NJ (1991); also as Rep. PPPL-2797, Princeton
      Plasma Physics Laboratory, Princeton, NJ (1991).

[9]   TANI, K., "Ripple loss of charged fusion products in TFTR
      and JT-60U", in Proc. of the First Workshop on Alpha
      Physics in TFTR, Princeton, NJ, 1991, unpublished.

[10] ZWEBEN, S.J., BIGLARI, H., Fusion Technol. 20 (1991)
      377.

[11] WHITE, R.B., MYNICK, H.E., Phys. Fluids B 1 (1989)
      980.

[12] GRUA, P., Confinement des Ions Suprathermiques dans
      un Tokamak Non Axisymmétrique, PhD thesis,
      Université Aix-Marseilles I, Provence (1989); also as
      Rep. EUR-CEA-FC 1385, Association Euratom–CEA,
      Centre d'études de Cadarache, Saint Paul-lez-Durance
      (1989).

[13] GRUA, P., ROUBIN, J.-P., Nucl. Fusion 30 (1990) 1499.

[14] DUVALL, R.E., Topics in Action-Angle Methods Applied
      to Tokamak Transport and Multiphoton Excitation of Atomic
      Systems, PhD Thesis, Princeton University, Princeton, NJ
      (1990).

[15] FELT, J., BARNES, C.W., CHRIEN, R.E., et al.,
      Rev. Sci. Instrum. 61 (1990) 3262.

[16] WHITE, R.B., CHANCE, M.S., Phys. Fluids 27 (1984)
      2455.

[17] WHITE, R.B., Phys. Fluids B 2 (1990) 845.

[18] FOIT, J.J., TANI, K., TAKIZUKA, T., AZUMI, M.,
      Mapping Model for Trapped Particles in a Toroidal Ripple
      Field, Tech. Rep. JAERI-M 88-249, Japan Atomic Energy
      Research Institute (1988).

[19] BITTONI, E., HAEGI, M., Fusion Technol. 18 (1990) 373.

[20] HIVELY, L.M., Nucl. Fusion 24 (1984) 779.

[21] HIVELY, L.M., Fusion Technol. 13 (1988) 438.

[22] TANI, K., TAKIZUKA, T., AZUMI, M., KISHIMOTO, H.,
      Nucl. Fusion 23 (1983) 657.

[23] BOIVIN, R.L., LIN, Z., ROQUEMORE, A.L.,
      ZWEBEN, S.J., Rev. Sci. Instrum. 63 (1992) 4418.

[24] ZWEBEN, S.J., BOIVIN, R.L., DIESSO, M., et al.,
      Nucl. Fusion 30 (1990) 1551.

[25] BOIVIN, R.L., KILPATRICK, S., MANOS, D.,
      ZWEBEN, S.J., Rev. Sci. Instrum. 61 (1990) 3208.

[26] STRACHAN, J.D., Nucl. Fusion 16 (1976) 743.

[27] ROQUEMORE, A.L., CHOUINARD, R.C., DIESSO, M.,
      et al., Rev. Sci. Instrum. 61 (1990) 3163.

[28] TOWNER, H., GOLDSTON, R., HAMMETT, G., et al.,
      Rev. Sci. Instrum 63 (1992) 4753.

[29] ZWEBEN, S.J., Nucl. Fusion 29 (1989) 825.

[30] ZWEBEN, S.J., BOIVIN, R.L., CHANG, C.-S.,
      HAMMETT, G.W., MYNICK, H.E., Nucl. Fusion 31
      (1991) 2219.

[31] SCOTT, S.D., BARNES, C.W., GRISHAM, L.R., et al.,
      in Plasma Physics and Controlled Nuclear Fusion Research
      1990 (Proc. 13th Int. Conf. Washington, DC, 1990), Vol. 1,
      IAEA, Vienna (1991) 235.

[32] HAWRYLUK, R.J., in Physics of Plasmas Close to
      Thermonuclear Conditions (Proc. Course Varenna, 1979),
      Vol. 1, CEC, Brussels (1980) 19.